FREQUENCY DOMAIN ANALYSIS OF ELECTROTONIC COUPLING BETWEEN LEECH RETZIUS CELLS

J. YANG AND K. M. CHAPMAN
Neurosciences Section, Division of Biology and Medicine, Brown University, Providence, Rhode Island 02912

ABSTRACT Transfer functions of the input impedance $Z(f)$ and coupling ratio $H(f)$ were measured from the paired Retzius cells of leech segmental ganglia, using sinusoidal and pseudorandom test currents. The data were compared with two classes of linear electric circuit models of electrotonic coupling, one with a purely resistive junction, and the other with a finite equivalent cable coupling the two somata. Model simulations suggested the phase behavior of the coupling ratio as a sensitive discriminator between these two cases. For resistive coupling, the phase of the coupling ratio asymptotically approaches $-90°$ at high frequencies, while for a cable segment, at least 0.5 length constants in length, it crosses $-90°$ with a definite negative slope and continues to more negative values. Measured phase lags of the coupling ratio in Retzius cell preparations consistently exceeded $-90°$ at frequencies above 50 Hz, and phase plots crossed $-90°$ with significantly negative slopes. We conclude therefore that a significant cable segment contributes to the coupling between Retzius cell somata.

INTRODUCTION

The paired Retzius (R) cells within each segmental ganglion of the leech are coupled by a nonrectifying electrotonic junction (Hagiwara and Morita, 1962; Eckert, 1963; French and DiCaprio, 1975). Investigations of the permeability of this junction have shown that small molecules such as amino acids, nucleotides, and monosaccharides pass from one R cell to another without first leaking into the extracellular space (Globus et al., 1973; Reske et al., 1975). Despite this readily demonstrable physiological coupling, gap junctions between R cells have not been identified morphologically. However, fluorescent dye and horseradish peroxidase injections into both somata reveal extensive overlap in the neuropilar arborizations of the two cells (Lent, 1973; Smith et al., 1975; Mason and Leake, 1978). Such data suggest that the coupling may occur by direct contacts between terminals of the more remote arborizations, and that its electrotonic effects may therefore show some cablelike properties. This question was investigated earlier by French and DiCaprio (1975), by examining the frequency response of electrotonus using white noise test currents, and by an analysis of spike latencies. They concluded that the coupling between Retzius cells is essentially resistive, and represents gap junctions that are therefore electrically close to the two cell somata.

In the course of an investigation of other aspects of R-cell electrophysiology, however, consistent deviations from purely resistive coupling became apparent (Yang, 1982). The present study was therefore undertaken to reexamine the coupling problem in greater detail. Our experimental approach was similar to French and DiCaprio's, utilizing sinusoidal (SIN) and pseudorandom (PRS) test currents to determine transfer functions of the input impedance, $Z(f)$, and the coupling ratio, $H(f)$, for R cells in the resting state. These transfer functions were then compared with the corresponding properties of four theoretical models, two with purely resistive coupling (models 1 and 3), and two with cable coupling (models 2 and 4).

On the basis of the behavior at high frequencies of the phase of the coupling ratio $H(f)$, and of the magnitude attenuation of the input impedance $Z(f)$, we conclude that cable-coupled models better describe the electrotonic coupling between R cells. In a preliminary study (Chapman and Yang, 1982), we have also estimated quantitatively some of the geometrical and electrical parameters of the R-cell membrane and its equivalent short coupling cable, by further analyzing these same data.

THEORY

This section presents analytical expressions for the experimentally measurable transfer functions, the input impedance, $Z(f)$, and the coupling ratio $H(f)$, with which we describe the electrotonic coupling between the paired R cells (Table II). Four electrical equivalent circuit models are considered (Fig. 1). Derivations are outlined in the Appendix (Eqs. A1–A19), and the general behavior of models 1 and 2 is illustrated in Figs. 2 and 3. Our symbol usage (Table I) generally follows that of Hodgkin and Rushton (1946), and Jack et al.(1975). Throughout this discussion, we refer to the cell into which test current was injected as the driven (d) cell, and the opposite one as the follower (f) cell.

Dr. Yang's present address is University of Connecticut Medical School, Farmington, CT. Correspondence should be sent to Dr. Chapman.

TABLE I
LIST OF SYMBOLS

Symbol	Definition	Defining equation
a	cable radius (cm)	
b	soma radius (cm)	
C	soma membrane capacitance (μF)	
C_m	membrane specific capacitance (μF/cm^2)	
d	driven cell (subscript)	
f	frequency (Hz)	
f	follower cell (subscript)	
$H(S)$	coupling ratio V_f/V_d	4
I	test current (A)	
I_a	intracellular axial current (A)	A5
l	length of finite cable segment (cm)	
L	normalized cable length l/λ	
r_a	axial resistance per unit length (Ω/cm)	
R_a	resistivity of cytoplasm (Ω cm)	
R_m	membrane specific resistance (Ω cm^2)	
R_1	soma membrane resistance (Ω)	
R_2	coupling resistance (Ω)	
S	normalized complex frequency	1
t	time (s)	
T	normalized time, t/τ	
T	arbitrary cable termination (subscript)	
V_d	electrotonic potential at driven cell soma (V)	
V_f	electrotonic potential at follower cell soma (V)	
x	distance along cable (cm)	
X	normalized distance along cable, x/λ	
$Z(S)$	input impedance at driven cell (Ω)	3
Z_{cab}	input impedance of hemi-infinite cable (Ω)	A8
$Z_{L,T}$	input impedance of finite, terminated cable (Ω)	A10
Z_{soma}	transmembrane impedance of soma alone (Ω)	5
Z_T	arbitrary termination impedance	
λ	length constant of cable (cm)	6
ρ	soma/hemi-infinite cable resistance ratio	7
τ	membrane time constant R_mC_m(s)	2

In all models, the cell somata are represented by two simple lumped resistance-capacitance (RC) networks. The electrotonic coupling is modeled as a resistive junction in models 1 and 3, and as a finite cable segment in models 2 and 4. Models 1 and 2 differ from 3 and 4 in that the latter pair include electrical loading due to those portions of axonal arborization not directly involved in coupling the R-cell somata.

We use the common simplifying assumption that a branching axonal arborization can be represented as a single equivalent cable (Rall, 1959, 1977; Jack et al., 1975). This assumption requires that at each branch point the output impedance of the parent cylinder equals the parallel input impedance of all branches. This condition can be met when the 3/2 power of the diameter of the parent cylinder equals the sum of the 3/2 powers of the branch diameters (Rall, 1959). For a symmetric bifurcation, each branch diameter must therefore be 63% of that of the parent cylinder. Histological work on several neuronal types shows axonal branching consistent with this "3/2 power law" (Lux et al., 1970; Barrett

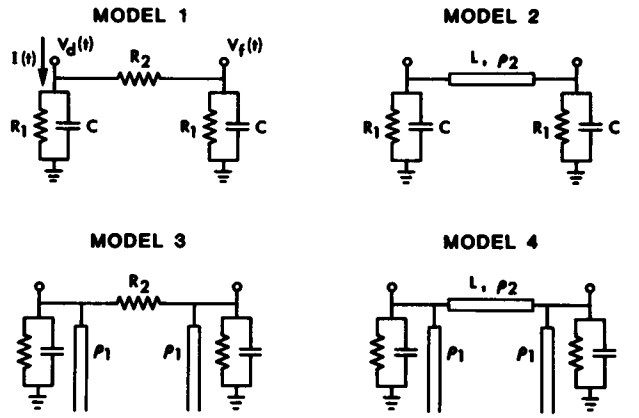

FIGURE 1 Four equivalent circuit models for the electrotonically coupled Retzius cells. The two somata are represented by parallel R_1C circuits in each case. Electrontonic coupling is purely resistive in models 1 and 3, represented by gap junction resistance R_2. An equivalent short cable segment of length constant λ_2 and electrotonic length L (rectangle) couples the cells in models 2 and 4. Models 3 and 4 include an equivalent hemi-infinite cable (open vertical rectangles) at each soma, representing all axonal and dendritic processes of each cell that do not participate in coupling to the opposite Retzius cell. Test current $I(t)$, and driven and follower cell electrotonic potentials $V_d(t)$ and $V_f(t)$ are identified in model 1.

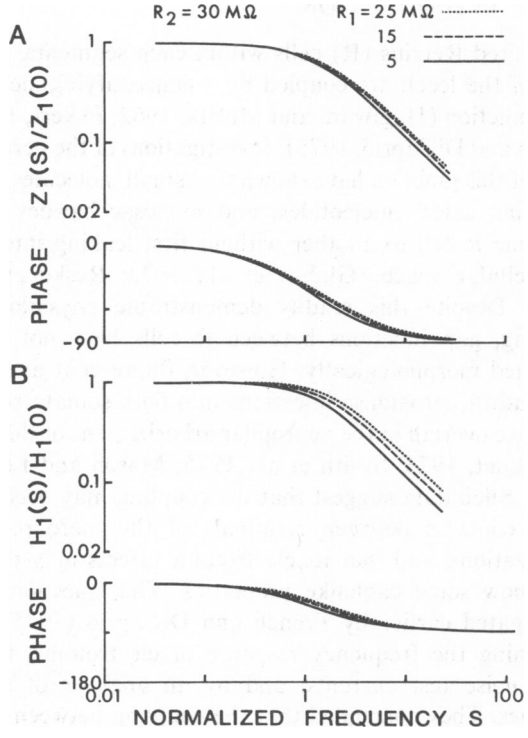

FIGURE 2 Model 1 simulations of input impedance $Z_1(S)$ (A) and coupling ratio $H_1(S)$ (B), as Bode plots (log magnitude, and phase in degrees, vs. log frequency). Magnitudes have been normalized with respect to their values at zero frequency, and frequency S with respect to the membrane time constant (Eq. 1). Coupling resistance R_2 = 30 MΩ in all cases. Soma resistance (in megaohms) R_1 = 25, (· · ·), 15, (---), and 5 (—). Both $Z_1(S)$ and $H_1(S)$ show first-order, low-pass behavior, with asymptotic magnitude attenuation slopes of −1, and asymptotic phase shifts of −90° at high frequency. Increasing R_1 while holding R_2 constant shifts the apparent corner frequency to the right.

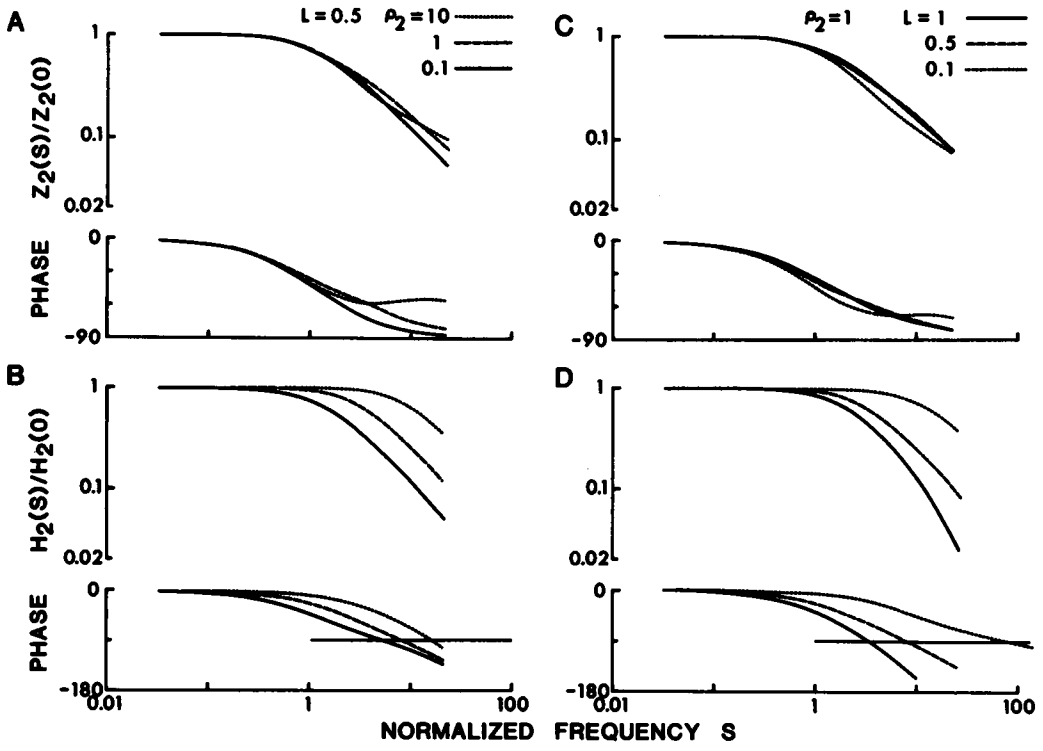

FIGURE 3 Model 2 simulations of input impedance $Z_2(S)$ (*A* and *C*) and coupling ratio $H_2(S)$ (*B* and *D*). Bode plots normalized as in Fig. 2. R_1 = 15 MΩ throughout. *A* and *B*, normalized cable length L = 0.5. ρ_2 = 10, (· · ·), 1, (---), and 0.1 (—). *C* and *D*, ρ_2 = 1. L = 0.1, (· · ·), 0.5, (---), and 1 (—). $H_2(S)$ phase angles exceed −90° at high frequencies, and cross −90° (indicated by line) with negative slope. Data summarized in Table III.

TABLE II
INPUT IMPEDANCES AND COUPLING RATIOS IN TERMS OF MODEL PARAMETERS

	Equation No.	Derived
Input impedances		
$Z_1(S) = \dfrac{R_1[R_1 + R_2(S+1)]}{2R_1(S+1) + R_2(S+1)^2}$	8	A12
$Z_2(S) = \dfrac{R_1[\rho_2 + \sqrt{S+1}\tanh(L\sqrt{S+1})]}{2\rho_2(S+1) + \sqrt{S+1}\tanh(L\sqrt{S+1})(\rho_2^2 + S + 1)}$	9	A14
$Z_3(S) = \dfrac{R_1[R_1 + R_2(\rho_1\sqrt{S+1} + S + 1)]}{2R_1(\rho_1\sqrt{S+1} + S + 1) + R_2(\rho_1\sqrt{S+1} + S + 1)^2}$	10	A16
$Z_4(S) = \dfrac{R_1[\rho_2 + (\rho_1 + \sqrt{S+1})\tanh(L\sqrt{S+1})]}{2\rho_2(\rho_1\sqrt{S+1} + S + 1) + \sqrt{S+1}\tanh(L\sqrt{S+1})[\rho_2^2 + (\rho_1 + \sqrt{S+1})^2]}$	11	A18
Coupling ratios		
$H_1(S) = \dfrac{R_1}{R_1 + R_2(S+1)}$	12	A13
$H_2(S) = \dfrac{\rho_2}{\rho_2 + \sqrt{S+1}\tanh(L\sqrt{S+1})}\operatorname{sech}(L\sqrt{S+1})$	13	A15
$H_3(S) = \dfrac{R_1}{R_1 + R_2(\rho_1\sqrt{S+1} + S + 1)}$	14	A17
$H_4(S) = \dfrac{\rho_2}{\rho_2 + (\rho_1 + \sqrt{S+1})\tanh(L\sqrt{S+1})}\operatorname{sech}(L\sqrt{S+1})$	15	A19

and Crill, 1971, 1974; Christensen and Teubl, 1979; Hillman, 1979) while others diverge or converge relative to this special geometry. Because detailed morphological data on the R-cell branching pattern are not available, we proceed with the 3/2 power law as a plausible working assumption. In particular, we treat the coupling arborization as a single, finite, equivalent cable segment, and all other branches of each cell as a second, hemi-infinite, equivalent cable. We also assume that the two cells are symmetrical, that their somata are spherical, that specific membrane characteristics R_m and C_m are uniform everywhere, and that all extracellular current densities are negligible.

Transfer functions were derived and computed in terms of normalized complex frequency S.[1] The imaginary part of S corresponds to the practical cyclic frequency f in Hz, normalized with respect to the membrane time constant, as

$$S = 0 + j\,2\pi f\tau \tag{1}$$

where

$$\tau = R_m C_m = R_1 C. \tag{2}$$

The desired transfer functions $Z(S)$ and $H(S)$ are defined as follows. The input impedance at the driven cell,

$$Z(S) = V_d(S)/I(S), \tag{3}$$

is the ratio of the electrotonic potential $V_d(S)$ of the driven cell soma to the injected test current $I(S)$. The coupling ratio

$$H(S) = V_f(S)/V_d(S) \tag{4}$$

is the ratio of the electrotonic potential $V_f(S)$ of the follower cell soma to that of the driven cell.

The input impedances for the four models are derived in the Appendix as series and/or parallel combinations of four basic elements: (*a*) a parallel R_1C network representing the soma, with impedance

$$Z_{soma}(S) = R_1/(S + 1) \tag{5}$$

(*b*) the resistance R_2 representing the gap junctions in models 1 and 3; (*c*) a hemi-infinite cable with impedance $Z_{cab1}(S)$ (Eq. A8) representing the noncoupling axonal arborizations in models 3 and 4; and (*d*) a cable segment of finite length l, terminated by the soma of the follower cell, representing cable coupling in models 2 and 4 (Eq. A10). The cable length constant is given by

$$\lambda = (a\,R_m/2\,R_a)^{1/2}. \tag{6}$$

Cable components are also described in terms of the soma/hemi-infinite cable resistance ratio ρ (Rall, 1959):

$$\rho = R_1/r_a\,\lambda = (a^3\,R_m/8\,b^4\,R_a)^{1/2}. \tag{7}$$

The noncoupling arborization in models 3 and 4 is denoted by ρ_1, λ_1, and Z_{cab1}; and the hemi-infinite case of the coupling segment in models 2 and 4 by ρ_2, λ_2, and Z_{cab2}.

Coupling ratios $H(S)$ were derived by ordinary network principles for resistively coupled models 1 and 3, and from expressions for the electrotonic cable potential $V(X,S)$ (Eq. A6) and the axial cable current $I_a(X,S)$ (Eq. A7), which arise in the derivations of the cable impedances.

Expressions for $Z(S)$ and $H(S)$ for the four models, designated by respective subscripts, are derived in terms of the basic equivalent circuit elements in the Appendix (Eqs. A2–A9), and are expressed in terms of model parameters R_1, R_2, L, ρ_1, ρ_2, and S in Table II (Eqs. 8–15).

Model Simulation

Input impedances and coupling ratios for the circuit models of Fig. 1 were computed and plotted as normalized Bode plots, both to illustrate their general behavior, and as an aid in designing experimental tests for the nature of coupling. Magnitudes were normalized on their values at low frequency, and frequency was normalized as defined in Eq. 1. Model parameters were varied systematically to explore their effects, and the most critical were studied in further detail.

Normalized Bode plots for models 1 and 2 are shown in Figs. 2 and 3, respectively. The midrange parameter values chosen were soma resistance R_1 = 15 M , model 1 coupling resistance R_2 = 30 M, model 2 normalized cable length L = 0.5, and ρ_2 = 1. The ranges examined for R_1 and R_2 were based on French and DiCaprio's (1975) data, while those for L and ρ_2 were chosen to give adequate variation about realistic values for a dendritic radius a = 2 μm, soma radius b = 30 μm, specific membrane resistivity R_m = 1,000 Ω cm^2, and specific axoplasmic resistivity R_a = 100 Ω cm. Membrane capacitance C_m was not varied, since it does not affect the shapes of the normalized Bode plots.

Fig. 2 shows the behavior of model 1 for three values of R_1. Both $Z_1(S)$ and $H_1(S)$ have the same asymptotic behavior at low and high frequency. Both become constant with zero phase shift at DC, and approach magnitude slopes of -1 with phase shifts of $-90°$ at high frequency. This is essentially the behavior of a first-order, low-pass system. As R_1 increases relative to R_2, both transfer functions shift to the right. However, for the fivefold range of R_1 shown, this effect is small. The first-order asymptotic behavior of Z_1 and H_1 is in fact independent of the model parameters.

Fig. 3 shows the behavior of model 2 for three values each of ρ_2 and L. With ρ_2 taken as independent, normalization eliminates R_1 from both $Z_2(S)$ and $H_2(S)$, so that R_1 has no effect on the shapes of these curves. For the higher frequencies shown, $Z_2(S)$ differs in detail from the first-order, low-pass character of $Z_1(S)$. For still higher frequencies, however, Eqs. 8 and 9 indicate that Z_2 approaches the asymptotic behavior of Z_1. In the frequency range of interest, larger values of ρ_2 or L emphasize the cable contribution to the input impedance in these cases, the slope of the magnitude attenuation becomes less steep, and the phase lag becomes both less negative, and nonmonotonic (Fig. 3, *A* and *C*). However, these differences proved to be too small to provide a useful experimental criterion for distinguishing the two models.

On the other hand, coupling ratio $H_2(S)$ shows notable differences from $H_1(S)$ in magnitude, and especially in phase behavior. As ρ_2 decreases in Fig. 3 *B*, or L increases in Fig. 3 *D*, the impedance of the cable segment becomes more important in the coupling ratio. In these cases, the magnitude attenuates with a slope steeper than -1 at high frequencies, and phase lags greater than $-90°$ occur such that the phase plot crosses $-90°$ with a distinctly negative slope. This effect is shown clearly for values of $L > 0.5$ in Fig. 3 *D*. The asymptotic behavior of $H_2(S)$ for large values of S (Eq. 13) is that the phase lag continues toward minus infinity, while the slope of magnitude attenuation returns to the cable value of $-1/2$.

The phase behavior of the coupling ratio provided the most powerful experimental test for a cable contribution in the coupling between the Retzius cells.

Simulations were also computed for models 3 and 4 (Eqs. 10, 11, 14, 15). Those for model 4 were done with $\rho_1 = \rho_2$ only. The added hemi-infinite cable load due to the noncoupling arborization introduced little change in the general qualitative behavior of either transfer function, except to introduce nonmonotonic phase behavior into the input impedance $Z_3(f)$ of resistively coupled model 3. As can be seen in Table II, models 3 and 4 approach models 1 and 2, respectively, at high frequency; that is, the noncoupling arborizations become unimportant. Because models 3 and 4 did not contribute any further insight into the nature of coupling, we did not consider them further.

[1]For economy of notation, we use $Z(f)$ and $H(f)$ to denote the expressions that result from $Z(S)$ and $H(S)$ when S is replaced by the right-hand side of Eq. 1. Except in the Appendix, we similarly use the arguments S, F, and T interchangeably in the expressions for V and I. Context and the form of the argument imply the intended form of the expression.

MATERIALS AND METHODS

Experiments were conducted on the American leech *Macrobdella decora*. The leeches were obtained commercially and kept in artificial pond water at 10°C until used. Ganglia were dissected and mounted as described earlier (Stuart, 1970; Yang and Lent, 1983). Leech Ringer's solution with elevated calcium (116 mM NaCl, 4 mM KCl, 8 mM CaCl, 12 mM glucose, 10 mM Tris maleate; pH 7.4) was used to stabilize the preparation.

Transfer functions of input impedance $Z(f)$ and coupling ratio $H(f)$ were determined by injecting sinusoidally or PRS-modulated subthreshold test current into the soma of the driven (d) cell and measuring the electrotonic potentials from both somata (Fig. 4). Three microelectrodes were used, two in the driven cell and one in the follower (f) cell. Microelectrodes were filled with 2 M K-acetate, and had tip resistances of ~20 MΩ. Voltages were recorded with conventional electrometer amplifiers (W.-P. Instruments, Inc., New Haven, CT, model M4A). Driven cell voltage $V_d(t)$, follower cell voltage $V_f(t)$, test current $I(t)$, and a time reference pulse were recorded on a four-channel FM tape recorder (Hewlett-Packard Co., Palo Alto, CA, model 3900), and were later replayed into three 10-bit analog-to-digital converters and a clock input of a PDP-12 computer (Digital Equipment Corp., Marlboro, MA) for off-line analysis.

Test Currents

SIN- and PRS-modulated test currents were chosen to give transfer functions on the approximate frequency range 0.5–64 Hz. Two signal sources were used: a conventional sine wave generator (Krohn-Hite Corp., Avon, MA, KH5200B), and a specialized pseudorandom binary sequence (PRS) generator designed to produce a periodic noise signal with a 2 s repeat period and a well-defined power spectrum. The PRS generator comprised an eight-bit universal shift register (SN74198) with XOR feedbacks (SN7486), filtered through a sixth-order, active, low-pass filter. These voltage signals were used to modulate a voltage-controlled current source, which produced the actual test current. To avoid local responses or spiking, which could have compromised passive membrane conditions, the DC levels of the test currents were adjusted to hyperpolarize the cells by ~10–20 mV. This was sufficient to permit adequate signal-to-noise ratio, while avoiding active responses.

Data Sampling and Analysis

The SIN experiments were performed and analyzed essentially as described previously for another system (Chapman and Duckrow, 1975). Sinusoidal signals at each frequency were sampled and the successive periods averaged for 5 s plus the remainder of the current period. A best-fitting sinusoid with the same frequency was computed immediately for $I(t)$, $V_d(t)$ and $V_f(t)$, giving estimates of mean level, peak amplitude, and phase relative to the time reference pulse for each signal. Transfer functions for input impedance $Z(f)$ (Eq. 3) and coupling ratio $H(f)$ (Eq. 4) were computed later, as the amplitude ratios and phase differences of the respective signals. Though adequate, this rather laborious SIN approach required typically 10–20 min to cover the desired frequency range,and entailed the risk of cell deterioration or loss of electrode impalement before the series was competed.

For the PRS experiments, modulated signals $I(t)$, $V_d(t)$, and $V_f(t)$ were each sampled to give 256 points per 2 s repeat period, and were averaged for 10 successive periods. Fourier transforms of the averaged time signals were computed immediately by a fast Fourier transform (FFT) algorithm, giving the mean and 127 harmonic terms on the range 0.5–63.5 Hz for each signal. Transfer functions $Z(f)$ and $H(f)$ were computed off-line as for the SIN data. As a further aid to graphical analysis, these raw transfer function estimates were smoothed by averaging three to four successive raw estimates. The great advantage of the PRS approach was that the entire frequency range could be tested in little more than the time required to sample the lowest frequency in SIN experiments, or in ~20–60 s for PRS as opposed to 10–20 min for SIN. PRS modulation was therefore used extensively in all of the later experiments.

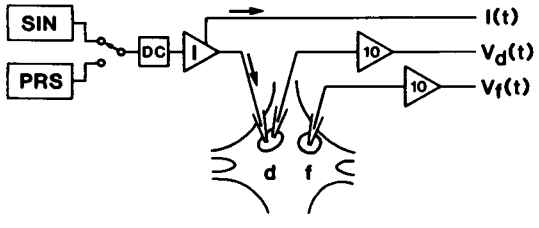

FIGURE 4 Diagram of the experimental arrangement. SIN- or PRS-modulated test currents $I(t)$ enter the driven cell (d) through one microelectrode, and electrotonic potentials $V_d(t)$ of the driven cell and $V_f(t)$ of the follower cell (f) are measured by an additional microelectrode in each cell. DC offset to the current source I provides hyperpolarization to avoid excitatory responses.

RESULTS

Experimental results were obtained from 15 ganglion preparations, using sinusoidal test currents in six cases, and PRS modulation in 14 cases. Representative data records are shown in Fig. 5 (SIN) and Fig. 7 (PRS).

The traces in Fig. 5 from top to bottom are driven-cell potential $V_d(t)$, follower-cell potential $V_f(t)$, and test current $I(t)$, modulated sinusoidally at frequencies 1, 6.5, and 40 Hz. Comparison shows large attenuation of $V_f(t)$ and a smaller decrease of $V_d(t)$ at higher frequencies, for a constant $I(t)$ modulation amplitude. The limiting low frequency response, approximated by the signals at 1 Hz, shows an input impedance $Z(0)$ of 18 MΩ and a coupling coefficient $H(0)$ of 0.31. The phase relationships are barely detectable on this time scale, but are readily determined by computer analysis.

Figs. 6*A* and 6*B* are Bode plots of $Z(f)$ and $H(f)$ obtained in a typical SIN experiment. These typically consisted of 10–15 frequency readings ranging ~0.2–60 Hz. In both $Z(f)$ and $H(f)$, general low-pass behavior is seen, with somewhat steeper magnitude attenuation and distinctly greater phase lag for $H(f)$ than for $Z(f)$ at high frequencies.

Fig. 7 shows typical data records from a PRS experiment. As with the SIN experiment, comparison of $V_d(t)$,

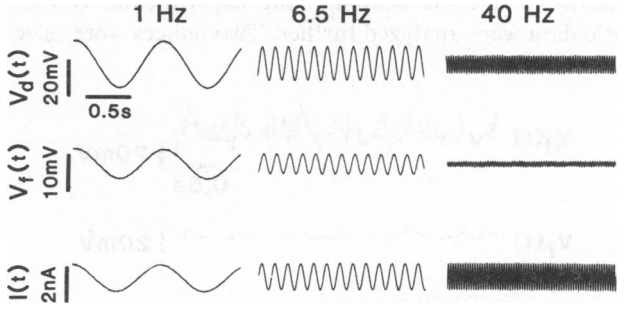

FIGURE 5 Representative data traces from a SIN experiment at three frequencies. Traces, *top* to *bottom*, driven cell potential $V_d(t)$, follower cell potential $V_f(t)$, test current $I(t)$. Hyperpolarizing DC offset not shown.

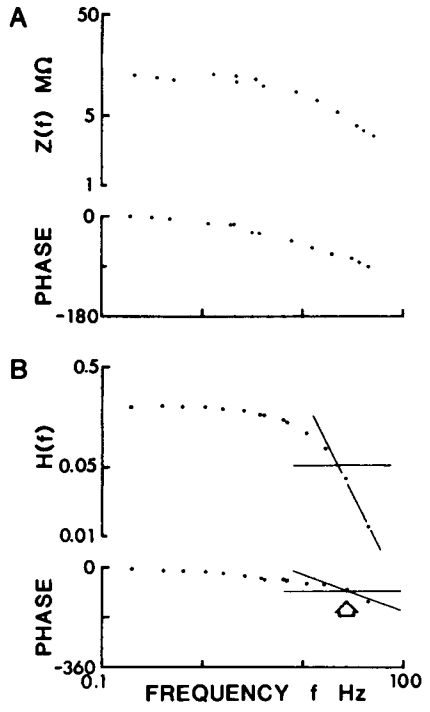

FIGURE 6 Experimentally determined Bode plots of input impedance $Z(f)$ (A), and coupling ratio $H(f)$ (B) from a representative SIN experiment. Phase of $H(f)$ crosses $-90°$ line at 50 Hz with a distinctly negative slope (arrow), and above 50 Hz the rate of $H(f)$ magnitude attenuation exceeds -1.

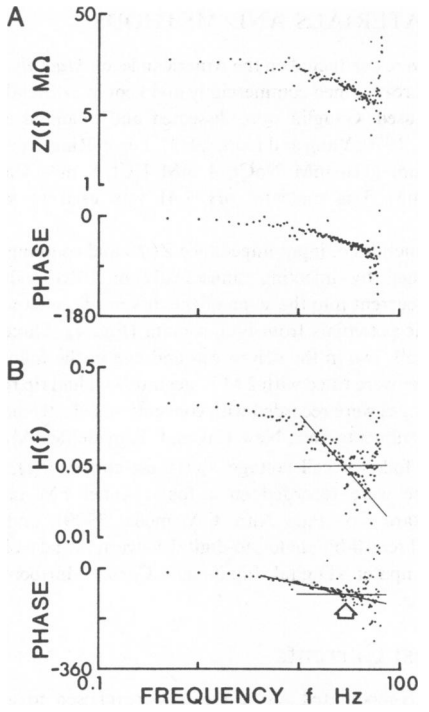

FIGURE 8 Unaveraged Bode plots of $Z(f)$ (A) and $H(f)$ (B) from a representative PRS experiment. Despite point scatter at high frequencies in these unaveraged transfer functions, coupling ratio phase is seen to cross $-90°$ with negative slope at 28 Hz (arrow), and attenuation of $H(f)$ magnitude appears to exceed -1 above 28 Hz.

$V_f(t)$, and $I(t)$ shows the general low-pass behavior of the input impedance and the coupling. Fig. 8 shows Bode plots of $Z(f)$ and $H(f)$ for the same PRS data, for 127 harmonic frequencies from 0.5 to 63.5 Hz. The transfer functions in this case have not been smoothed by averaging, and illustrate the considerable scatter that occurs at higher frequencies, due to the small signal-to-noise ratios as $V_d(t)$ and $V_f(t)$ attenuate. Despite this scatter, the qualitative properties of these transfer functions agree with those of Fig. 6. It is evident that $H(f)$ attenuates faster than $Z(f)$, and that the limiting phase lag of $H(f)$ exceeds $-90°$ at high frequencies.

Because the asymptotic behavior of $H(s)$ in the model simulations suggested a sensitive discrimination between resistive and cable coupling, the experimental coupling ratio data were analyzed further. Two indices were selected, and were read from the Bode plots of each experiment: (a) the slope of the magnitude plot at high frequency [see slope $H(f)$, Fig. 9 A], and (b) the slope of the phase plot as the phase angle approaches or crosses $-90°$ [$\angle H(f)$, Fig. 9 B]. Initially, slope analyses were done by log-linear regression, but slopes measured in this way proved to be indistinguishable from those estimated visually from Bode plots that had been smoothed by averaging.

Fig. 9 shows histograms of the two slopes for all

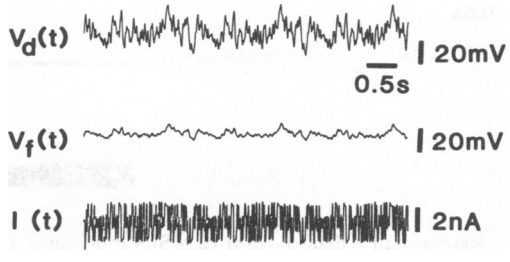

FIGURE 7 Representative data traces from a PRS experiment. Traces identified as in Fig. 5. DC offset not shown.

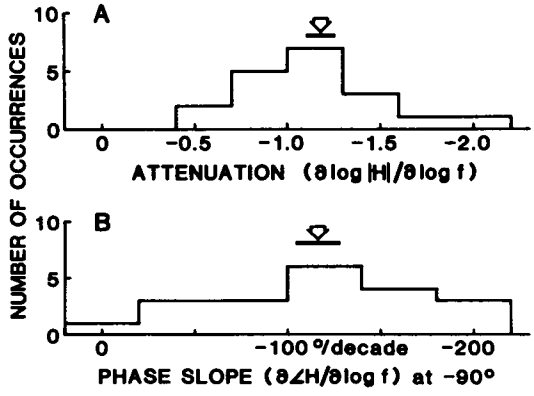

FIGURE 9 Histograms of $H(f)$ attenuation slope at the highest frequencies tested (A), and slope of $H(f)$ phase at $-90°$ crossover (B), read from the experimental Bode plots of coupling ratios. Data from 20 measurements, 6 by SIN, 14 by PRS methods. Arrows indicate mean, bars indicate ± SEM.

determinations made in all preparations comprising this study. Slopes were measured visually from Bode plots of both SIN and PRS measurements. The mean slope of the magnitude attenuation at the highest frequencies tested (Fig. 9 *A*) was not significantly different from the value −1 expected for the resistively coupled model ($P = 0.06$), though the range was large and included preparations with slopes as steep as −2. As is seen in the simulation data for model 2 (Fig. 3 and Table III), the frequency beyond which cable attenuation exceeds −1 depends rather strongly on model parameters. Individual Bode plots were not tested separately, but it is very likely that a number of these slopes were significantly more negative than −1. However, when applied to the pooled data, this potentially useful criterion proved to be inconclusive for discriminating between resistive and cable coupling.

For the 20 determinations made, phase plots of the coupling ratio reached −90° within the frequency range tested, and all but one crossed −90° with appreciably negative slopes (Fig. 9 *B*). The average slope for the pooled data was −117° ± 12°/decade frequency, and was highly significantly different ($P << 0.001$) from the asymptotic slope of zero expected for the resistive model. This phase criterion therefore does discriminate successfully between the two models, and indicates that there is a clearly detectable cable contribution to electrotonic coupling between the two Retzius cell somata.

DISCUSSION

The question of resistive vs. cable coupling between Retzius cells is a qualitative one, but the theoretical and experimental techniques needed to resolve it are necessarily quantitative. Most of the theoretical effort in the present report was directed toward finding practical experimental tests, but it has also provided a basis for quantitative estimation of the parameters of at least one model that describes our data. This parameter estimation problem is the topic of a preliminary report (Chapman and Yang, 1982) and a later paper.

Our principal conclusion in the present report is that there is a significant cable component coupling the two R cells. In their earlier work, French and DiCaprio (1975) arrived at the opposite conclusion. Based on their band-limited white noise measurement of the coupling transfer function, and on their short-cable model simulation, they concluded that the coupling is essentially resistive, and differs dramatically from cable behavior. This disagreement is one of interpretation, rather than of methods or data. Our experimental approach to the electrotonus measurements was virtually identical to theirs, except for nonessential differences in test current waveforms, and that our frequency range (0.5–64 Hz) exceeded theirs (1.6–48 Hz; French and DiCaprio, 1975, Fig. 1) by about a half decade. Moreover, their Bode plot (their Fig. 1) for the coupling ratio is consistent with our own data. Their attenuation slope at 30–40 Hz for the experimental points is ~16% steeper than for the resistive model, and the phase points appear to cross −90° at ~30 Hz with a slope of about −50°/decade of frequency. These values are well within the ranges of our experimental transfer functions for $H(f)$ (Fig. 9), and are consistent with the behavior of $H(S)$ for our cable-coupled model 2 (Fig. 3). The differences between the experimetal data and the resistive model are admittedly rather subtle, and without adequate statistics could reasonably be dismissed as experimental error.

TABLE III
CRITICAL FEATURES OF MODEL 2 COUPLING RATIO $H_2(S)$

Parameters ρ	Parameters L	Attenuation slope $\partial\log\lvert H\rvert/\partial\log S$ at normalized frequency $S = 20$	Phase angle crossover frequency at −90° S	Phase angle crossover slope at −90°
				Deg/decade
1	0.1	−0.75	80.4	− 35
	1	−1.4	3.3	−126
10	0.5	−0.98	15.8	−122
1		−1.15	7.9	− 86
0.1		−1.2	5.6	− 59

Data from Fig. 3.

The differing conclusions from these two studies are due to an important difference in the cable models used. In our models 2 and 4 the finite cable segment is terminated by the impedance of the follower cell, whereas French and DiCaprio considered the open circuit termination only (our Eq. A11a). That case is an inappropriate model for the two cells, since there can then be no current passage, and hence no coupling between the two somata. Anatomically, the coupling branches would be detached from the follower cell soma, and their free ends sealed. Accordingly, French and DeCaprio's Eq. 22 gives the correct coupling ratio for the open-circuited end of the cable segment, but does not describe the electrotonic potential that would be seen at the follower cell soma with the coupling intact. Our expressions for $H_2(S)$ (Eqs. 13 and A15) reduce to their Eq. 22 when Z_{soma} and ρ_2 are infinite. Those for $H_4(S)$ (Eqs. 15 and A19) do so as well when, in addition, Z_{soma}/Z_{cab1}, and ρ_1 are both finite.

French and DeCaprio (1975) are quite correct in modeling the gap junctions as essentially resistive, however. We have omitted the gap junctions from our models 2 and 4, where they should properly appear as a single resistance interrupting the cable segment at its midpoint, at $L/2$. The cable segment itself does approach a simple resistance equivalent to R_2 for short lengths, since the short-circuited cable segment impedance Z_{L0} (Eq. A11b) reduces to $R_a l = R_2$ for L less than ~0.1. If the cable diameter is also shrunk so that ρ_2 becomes less than ~0.1, then $Z_2(S)$ and $H_2(S)$ reduce to the model 1 case (Table II). However, the uninterrupted longer cable is not in

general equivalent to the resistively interrupted case. This point is considered further in a later paper.

The morphological correlates of cable coupling remain to be shown. But whether the branching pattern follows the 3/2 power law precisely or not, the fact that significant cable behavior can be detected implies that the gap junctions occur at some distance from the cell somata. It may be possble to estimate the number of gap junctions from electrophysiological data, but how they are distributed among the branches will probably have to be settled by morphological methods.

APPENDIX

The derivations of input impedance $Z(S)$ and coupling ratio $H(S)$ are outlined here for the four models of Fig. 1. Certain well-known results will be repeated where useful. In particular, expressions for the cable electrotonic potential and axial cable current in the frequency domain, and the impedance of a finite cable with arbitrary termination, are needed for models 2, 3, and 4, and will be derived first.

The electrotonic potential $V(X,T)$ for a quiescent, uniform cylindrical axon is given by the linear cable equation, expressed in normalized form (Hodgkin and Rushton, 1946; Jack et al., 1975, pp. 25–29):

$$\frac{\partial^2 V(X,T)}{\partial X^2} - \frac{\partial V(X,T)}{\partial T} - V(X,T) = 0 \qquad \text{(A1)}$$

in which normalized distance $X = x/\lambda$, and normalized time $T = t/\tau$. The point $X = 0$ is taken as the input point when considering input impedances. Eq. A1 is solved by two Laplace transformations. One is taken with respect to T, yielding relations that will be left in the normalized complex frequency domain S (Eq. 1). The second is taken with respect to X to give the second-order solution, which is then inverted, returning it to the X domain. The first and second Laplace transformations of V will be denoted $\overline{V}$ and $\overline{\overline{V}}$, respectively.

The Laplace transform of Eq. A1 with respect to T is

$$\frac{\partial^2 \overline{V}(X,S)}{\partial X^2} - (S+1)\,\overline{V}(X,S) + V(X,0) = 0 \qquad \text{(A2)}$$

in which the initial condition $V(X,0)$ at $T = 0$ is taken as 0; i.e., the system is treated as initially relaxed. Transforming Eq. A2 to the $q = 1/X$ domain yields

$$\overline{\overline{V}}(q,S) = \frac{q\,\overline{V}(0,S) + \partial\overline{V}(0,S)/\partial X}{q^2 - (S+1)}. \qquad \text{(A3)}$$

This on inversion (e.g., Beyer, 1978, p. 601, Nos. 17 and 18) gives the cable electrotonic potential in terms of its value and gradient at $X = 0$ (only one of which can be specified independently):

$$\overline{V}(X,S) = \overline{V}(0,S)\cosh(X\sqrt{S+1}) + \frac{\partial\overline{V}(0,S)}{\partial X}\frac{\sinh(X\sqrt{S+1})}{\sqrt{S+1}}. \qquad \text{(A4)}$$

The longitudinal axial cable current $\bar{I}_a(X,S)$ in the $+X$ direction is given by Ohm's law as

$$\bar{I}_a(X,S) = -\frac{1}{r_a\lambda}\frac{\partial\overline{V}(X,S)}{\partial X}. \qquad \text{(A5)}$$

Next, $\overline{V}(X,S)$ and $\bar{I}_a(X,S)$ are each expressed in terms of both $\overline{V}(0,S)$ and $\bar{I}_a(0,S)$ ($X = 0$ in Eq. A5 eliminates the gradient in Eq. A4, then differentiation yields the gradient for Eq. A5):

$$\overline{V}(X,S) = \overline{V}(0,S)\cosh(X\sqrt{S+1}) - \frac{r_a\lambda}{\sqrt{S+1}}\bar{I}_a(0,S)\sinh(X\sqrt{S+1}) \qquad \text{(A6)}$$

and

$$\bar{I}_a(X,S) = -\overline{V}(0,S)\frac{\sqrt{S+1}}{r_a\lambda}\sinh(X\sqrt{S+1}) + \bar{I}_a(0,S)\cosh(X\sqrt{S+1}). \qquad \text{(A7)}$$

Cable input impedances are derived from Eqs. A6 and A7 and $\overline{V}(0,S)/\bar{I}_a(0,S)$. Notation for impedance functions of S alone will usually be abbreviated by omitting the argument.

The well-known input impedance $Z_{cab}(S)$ of a hemi-infinite cable follows immediately from either Eq. A6 or A7 with infinite X, provided $\overline{V}(X,S)$ and $\bar{I}_a(X,S)$ remain finite for all X (Eq. A11c avoids this assumption):

$$Z_{cab}(S) = r_a\lambda/\sqrt{S+1} \qquad \text{(A8)}$$

The input impedance $Z_{L,T}(S)$ of a finite cable segment of length l and normalized length $L = l/\lambda$, terminated by an arbitrary impedance $Z_T(S)$, is also well known. It follows from the terminal constraint at $X = L$:

$$\overline{V}(L,S)/\bar{I}_a(L,S) = Z_T(S). \qquad \text{(A9)}$$

With $X = L$ in Eqs. A6 and A7, Eq. A9 yields the required ratio:

$$Z_{L,T}(S) = Z_{cab}\cdot\frac{Z_{cab}\sinh(L\sqrt{S+1}) + Z_T\cosh(L\sqrt{S+1})}{Z_{cab}\cosh(L\sqrt{S+1}) + Z_T\sinh(L\sqrt{S+1})}. \qquad \text{(A10)}$$

Special cases of interest are (*a*) Z_T = infinity, or "open circuit" termination:

$$Z_{L,\infty} = Z_{cab}\coth(L\sqrt{S+1}). \qquad \text{(A11a)}$$

(*b*) $Z_T = 0$, or "short circuit" termination:

$$Z_{L,0} = Z_{cab}\tanh(L\sqrt{S+1}). \qquad \text{(A11b)}$$

(*c*) L = infinity, the hemi-infinite cable [Eq. A8, without stipulating finite $\overline{V}(X,S)$ and $\bar{I}_a(X,S)$]:

$$Z_{\infty,T} = Z_{cab}. \qquad \text{(A11c)}$$

Derivations of $Z(S)$ and $H(S)$ for the four models are outlined next. The expressions are arranged to reduce to the simpler cases by inspection. Those given here (Eqs. A12–A19) are expressed in terms of the equivalent circuit elements of Fig. 1. Those in Table II (Eqs. 8–15) are in terms of the model parameters R_1, R_2, ρ_1, ρ_2, L, and S used in the simulations.

Model 1

The input impedance $Z_1(S)$ at the driven cell follows immediately from network principles, as the parallel combination Z_{soma} (driven) and R_2 in series with Z_{soma} (follower). Hence

$$Z_1(S) = \frac{Z_{soma}(Z_{soma} + R_2)}{2Z_{soma} + R_2}. \qquad \text{(A12)}$$

Coupling ratio $H_1(S)$ is given as a voltage divider network consisting of R_2 and Z_{soma} of the follower cell:

$$H_1(S) = \frac{Z_{soma}}{Z_{soma} + R_2}. \quad \text{(A13)}$$

Model 2

The input impedance at the driven cell soma is the impedance Z_{soma} of the driven cell in parallel with the impedance $Z_{L,soma}$ (Eq. A10) of the finite cable terminated by Z_{soma} of the follower cell. The combining form of the coupling segment arises as its short-circuit termination case (Eq. A11b), with additional terms:

$$Z_2(S) = \frac{Z_{soma}(Z_{soma} + Z_{L,0})}{2Z_{soma} + Z_{L,0}[(Z_{soma}/Z_{cab2})^2 + 1]}. \quad \text{(A14)}$$

Coupling ratio $H_2(S)$ follows directly from Eq. A6, with $\bar{V}(0,S)/\bar{I}_a(0,S) = Z_{L,soma}$:

$$H_2(S) = \frac{Z_{soma}}{Z_{soma} + Z_{L,0}} \operatorname{sech}(L\sqrt{S+1}). \quad \text{(A15)}$$

Model 3

$Z_3(S)$ follows from $Z_1(S)$, with Z_{soma} for both the driven and follower cell replaced by Z_{soma} in parallel with Z_{cabl}:

$$Z_3(S) = \frac{Z_{soma}[Z_{soma} + R_2(Z_{soma}/Z_{cabl} + 1)]}{2Z_{soma}(Z_{soma}/Z_{cabl} + 1) + R_2(Z_{soma}/Z_{cabl} + 1)^2}. \quad \text{(A16)}$$

Coupling ratio $H_3(S)$ follows similarly from $H_1(S)$:

$$H_3(S) = \frac{Z_{soma}}{Z_{soma} + R_2(Z_{soma}/Z_{cabl} + 1)}. \quad \text{(A17)}$$

Model 4

The parallel Z_{soma}-Z_{cabl} combinations of model 3 likewise replace Z_{soma} for the driven cell and for the follower-cell termination of the coupling segment in Eqs. A14 and A16:

$$Z_4(S) = \frac{Z_{soma}[Z_{soma} + Z_{L,0}(Z_{soma}/Z_{cabl} + 1)]}{2Z_{soma}(Z_{soma}/Z_{cabl} + 1) + Z_{L,0}[(Z_{soma}/Z_{cab2})^2 + (Z_{soma}/Z_{cabl} + 1)^2]} \quad \text{(A18)}$$

and

$$H_4(S) = \frac{Z_{soma}}{Z_{soma} + Z_{L,0}(Z_{soma}/Z_{cabl} + 1)} \cdot \operatorname{sech}(L\sqrt{S+1}). \quad \text{(A19)}$$

We thank C. M. Lent for providing facilities and for helpful discussion, P. A. Stewart for criticizing the manuscript, and R. Edwards for typing it.

The research for this paper was supported in part by U.S. Public Health Service–National Institutes of Health grant NS94482 to C. M. Lent.

Received for publication 28 April 1983 and in final form 24 June 1983.

Note added in proof: Peterson (1983, *Biophys. J.*, 43:53–61) has recently reported cable coupling between HE cells in the leech *Hirudo*.

REFERENCES

Barrett, J. N., and W. E. Crill. 1971. Specific membrane resistivity of dye-injected cat motoneurons. *Brain Res.* 28:556–561.

Barrett, J. N., and W. E. Crill. 1974. Specific membrane properties of cat motoneurones. *J. Physiol. (Lond.)* 239:301–324.

Beyer, W. H., editor. 1978. CRC Handbook of Mathematical Sciences. Fifth ed. CRC Press, Inc., Boca Raton, FL. 106.

Chapman, K. M., and R. B. Duckrow. 1975. Compliance and sensitivity of a mechanoreceptor of the insect exoskeleton. *J. Comp. Physiol.* 100:251–268.

Chapman, K. M., and J. Yang. 1982. Estimation of specific membrane and cable properties of leech Retzius cell electrotonic coupling. *Soc. Neurosci. Abstr.* 8:685.

Christensen, B. N., and W. P. Teubl. 1979. Estimates of cable parameters in lamprey spinal cord neurones. *J. Physiol.* 297:299–318.

Eckert, R. 1963. Electrical interaction of paired ganglion cells in the leech. *J. Gen. Physiol.* 46:573–587.

French, A. S., and R. A. DiCaprio. 1975. The dynamic electrical behavior of the electrotonic junction between Retzius cells in the leech. *Biol. Cybern.* 17:129–135.

Globus, H., H. D. Lux, and P. Schubert. 1973. Transfer of amino acids between neuroglia cells and neurons in the leech ganglion. *Exp. Neurol.* 40:104–113.

Hagiwara, S., and H. Morita. 1962. Electrotonic transmission between two nerve cells in leech ganglion. *J. Neurophysiol. (Bethesda).* 25:721–731.

Hillman, D. E. 1979. Neuronal shape parameters and substructures as a basis for neuronal form. *In* The Neurosciences: Fourth Study Program. F. O. Schmitt and F. G. Worden, editors. The MIT Press, Cambridge, MA. 477–498.

Hodgkin, A. L., and W. A. H. Rushton. 1946. The electrical constants of a crustacean nerve fibre. *Proc. R. Soc. Lond. B. Biol. Sci.* 133:444–479.

Jack, J. J. B., D. Noble, and R. W. Tsien. 1975. Electric Current Flow in Excitable Cells. Oxford University Press, London. xv–xvi.

Lent, C. M. 1973. Retzius' cells from segmental ganglia of four species of leeches: comparative neuronal geometry. *Comp. Biochem. Physiol. A. Comp. Physiol.* 44:35–40.

Lux, H. D., P. Schubert, and G. W. Kreutzberg. 1970. Direct matching of morphological and electrophysiological data in cat spinal motoneurones. *In* Excitatory Synaptic Mechanisms. P. Anderson and J. K. S. Jansen, editors. Universitetsforlaget, Oslo, Norway. 189–198.

Mason, A., and L. D. Leake. 1978. Morphology of leech Retzius cells demonstrated by intracellular injection of horseradish peroxidase. *Comp. Biochem. Physiol. A. Comp. Physiol.* 61:213–216.

Rall, W. 1959. Branching dendritic trees and motoneuron membrane resistivity. *Exp. Neurol.* 1:491–527.

Rall, W. 1977. Core conductor theory and cable properties of neurons. *In* Handbook of Physiology. E. Kandel, editor. American Physiological Society, Bethesda, MD. 1:39–97.

Reske, E., P. Schubert, and G. W. Kreutzberg. 1975. Transfer of radioactive material between electrically coupled neurons of the leech central nervous system. *Brain Res.* 84:365–382.

Smith P. A., A. J. Sunderland, L. D. Leake, and R. J. Walker. 1975. Cobalt staining and electrophysiological studies of Retzius cells in the leech, *Hirudo medicinalis. Comp. Biochem. Physiol. A. Comp. Physiol.* 51:655–661.

Stuart, A. E. 1970. Physiological and morphological properties of motoneurones in the central nervous system of the leech. *J. Physiol.* 209:627–646.

Yang, J. 1982. The effect of calcium depletion on the ionic conductance channels of the leech Retzius cell membrane. Ph.D. Dissertation, Brown University.

Yang, J., and C. M. Lent. 1983. Calcium depletion produces Na^+-dependent, sustained depolarizations of Retzius cell membranes in the leech CNS. *J. Comp. Physiol. A. Comp. Physiol.* 150:499–507.